GEOPHYSICS, VOL. 80, NO. 6 (NOVEMBER-DECEMBER 2015); P. K25–K36, 8 FIGS.
10.1190/GEO2015-0141.1

3D parametric hybrid inversion of time-domain airborne electromagnetic data

Michael S. McMillan[1], Christoph Schwarzbach[1], Eldad Haber[2], and Douglas W. Oldenburg[1]

ABSTRACT

We have developed a method to invert time-domain airborne electromagnetic (AEM) data using a parametric level-set approach combined with a conventional voxel-based technique to form a parametric hybrid inversion. The approach was designed for situations in which a voxel-based inversion alone may struggle. Such an example is where a distinct anomaly is present with sharp boundaries, and there is a large contrast between a low-resistivity target and a high-resistivity background. The first step of the proposed hybrid method used our novel parametric inversion to recover a best-fitting skewed Gaussian ellipsoid that represented the target of interest. Subsequently, the parametric result was set as an initial and reference model for the second stage, where smooth features with smaller resistivity contrasts were introduced into the model through a conventional voxel-based approach. The approach was tested with synthetic and field data. In the synthetic case, we recovered the size and dip of a conductive, thin, dipping plate with better accuracy compared with a voxel-based inversion. In the field example, we inverted AEM data over the Caber volcanogenic massive sulfide deposit. Based on information from past drilling, our results improve upon previous parametric plate inversions of the deposit itself, while additionally imaging the conductive cover over the deposit. These findings showcased how our parametric hybrid method can improve the accuracy of time-domain AEM inversions for thin dipping targets with large resistivity contrasts compared with the background.

INTRODUCTION

Airborne electromagnetics (AEM) is widely used as a mineral exploration tool for imaging subsurface distributions of electric resistivity. This physical property can identify rock types, mineralization, and alteration zones due to anomalous resistivity levels compared with background values (Keller, 1988). Resistivity and its reciprocal, conductivity, will be referred to in this paper. In a conventional voxel-based electromagnetic inversion, the resistivity value in every active mesh cell is solved with either a finite-difference (Commer and Newman, 2004), finite-volume (Haber et al., 2007b), or integral equation method (Cox et al., 2010). In recent years, as computational power has steadily increased, electromagnetic inversion algorithms have been modified to facilitate thousands of source locations. This has resulted in numerous 3D inversion codes being tailored to AEM data (Cox et al., 2012; Oldenburg et al., 2013; Haber and Schwarzbach, 2014).

However, when an anomaly of interest has sharp boundaries and a large contrast between a low-resistivity target and a high-resistivity background, our experience with voxel-based inversion codes is that they can encounter difficulties accurately defining these abrupt resistivity contrasts. Moreover, the true resistivity of the target is often overestimated, especially with a low-resistivity target. Therefore, in certain situations like this, there is a motivation to use a parametric method (Dorn et al., 2000; Dorn and Lesselier, 2006; van den Doel and Ascher, 2006). Here, instead of solving for the resistivity in every cell, only a few parameters are sought to describe the physical property space, and the reduction in the number of variables can typically be many orders of magnitude. Parametric inversions can also be coupled with such methods as level sets (Osher

Preliminary results presented at SEG 2014 in a talk entitled: "Recovering a thin dipping conductor with 3D electromagnetic inversion over the Caber deposit."
Manuscript received by the Editor 3 March 2015; revised manuscript received 10 July 2015; published online 28 September 2015.
[1]University of British Columbia, Geophysical Inversion Facility, Department of Earth, Ocean, and Atmospheric Sciences, Vancouver, British Columbia, Canada. E-mail: mmcmilla@eos.ubc.ca; cschwarz@eos.ubc.ca; doug@eos.ubc.ca.
[2]University of British Columbia Geophysical Inversion Facility, Department of Earth, Ocean, and Atmospheric Sciences. E-mail: ehaber@eos.ubc.ca.

and Sethian, 1988; Osher and Fedkiw, 2001) to solve for the resistivity and shape of a target of interest (Dorn and Lesselier, 2006; Aghasi et al., 2011). This produces a method of inverting for an anomaly with sharp boundaries and a high-resistivity contrast compared with the background with a minimal number of variables. This study adds to previous hybrid modeling approaches for AEM data, such as in Leroi Air (Raiche, 1998), in which thin sheet integral equations are used with 3D plates in a layered earth, and Marco Air (Xiong et al., 1995), in which volume integral equations are incorporated with 3D prisms in a layered earth.

Finding an appropriate parametrization is critical, and in this paper we have chosen to work with a skewed Gaussian ellipsoid to represent the target anomaly, although other options are available, such as radial basis functions or truncated Gaussian distributions (Aghasi et al., 2011; Pidlisecky et al., 2011). Our parametrization is chosen for its flexibility because it can easily discretize high-frequency features including plates and thin layers, as well as broader shapes such as large intrusions. However, we recognize that our parametrization has limitations, especially because it only recovers a single anomaly. Therefore, to account for additional features in the model space, the voxel-based phase of our method also solves for a smooth background. Our choice of parametrization is specific, but the method developed in this paper is general to any parametrization, and it could be applied to other geophysical data sets, such as potential fields, induced polarization, and frequency-domain electromagnetics. Furthermore, the paper focuses on airborne data, but the method is equally applicable to measurements acquired on the ground.

Our three research goals in this paper are as follows:

- to develop a parametric inversion for time-domain AEM data with a skewed Gaussian ellipsoid parametrization
- to show, with a synthetic and field example, that our parametric inversion can accurately recover a pertinent target for mineral exploration: a thin dipping plate
- to combine parametric and voxel-based inversion to form a hybrid technique that can model a single target of interest with parametric inversion, while filling in remaining features with a voxel-based code.

The paper first discusses general electromagnetic theory before going into detail on our parametric hybrid methodology. Simulated AEM data over a synthetic model composed of a thin dipping conductor in a resistive half-space are then introduced to provide a means to test our code. Following the synthetic example, our hybrid inversion is tested on AEM field data over a volcanogenic massive sulfide (VMS) deposit, and the results are compared with previous work and geologic knowledge from drilling.

ELECTROMAGNETIC BACKGROUND

Time-domain AEM experiments typically consist of a transmitter that carries a time-varying current that induces secondary currents in the ground. In turn, the induced currents have a secondary magnetic field that are measured by a receiver on an airborne platform. The process of electromagnetic induction is thoroughly discussed in many textbooks and will not be elaborated further (Ward and Hohmann, 1988; Nabighian and Macnae, 1991; Reynolds, 1998). This paper focuses on airborne platforms in which the receiver is contained in the center of the transmitter loop, known as *coincident loop systems* (Allard, 2007), and the data collected are typically x-, y-, z-component $\frac{\partial \mathbf{B}}{\partial t}$ data, where $\mathbf{B}$ is magnetic flux, although components of $\mathbf{B}$ alone can also be calculated.

For conventional voxel-based time-domain AEM inversions, we have chosen to follow the approach discussed in Haber and Schwarzbach (2014). This method uses Gauss-Newton-based optimization to solve quasi-static Maxwell's equations in space and time:

$$\nabla \times \mathbf{E} + \mu \frac{\partial \mathbf{H}}{\partial t} = 0, \tag{1}$$

$$\nabla \times \mathbf{H} - \sigma \mathbf{E} = \mathbf{s}, \tag{2}$$

subject to boundary and initial conditions

$$\mathbf{n} \times (\nabla \times \mathbf{H}) = 0, \tag{3}$$

$$\mathbf{H}(x, y, z, t = 0) = \mathbf{H}_0, \tag{4}$$

$$\nabla \cdot \mu \mathbf{H_0} = 0, \tag{5}$$

using a finite-volume discretization on OcTree meshes (Haber et al., 2007a). Here, $\mathbf{E}$ is a vector of electric fields, $\mathbf{H}$ is a vector of magnetic fields, μ is the magnetic permeability, σ is the electric conductivity, $\mathbf{s}$ is a source vector, $\mathbf{n}$ is a normal vector, x, y, z are spatial observation coordinates, and t is time. For further information on voxel-based electromagnetic inversion theory, see Haber et al. (2004, 2007b) and Haber and Heldmann (2007). We now proceed with our parametric hybrid inversion details.

INVERSION METHODOLOGY

Consider an inverse problem in which the forward problem has the form

$$F(m(\mathbf{x})) + \boldsymbol{\epsilon} = \mathbf{d}, \tag{6}$$

where F maps the function $m(\mathbf{x})$, with position vector $\mathbf{x}$, to the discrete data $\mathbf{d}$, and $\boldsymbol{\epsilon}$ is the noise that is assumed to be Gaussian with a known covariance matrix $\boldsymbol{\Sigma}_d$. After discretization of the model, we obtain a discrete problem:

$$F(\mathbf{m}) + \boldsymbol{\epsilon} = \mathbf{d}, \tag{7}$$

where $\mathbf{m}$ is a discrete approximation to the function $m(x)$. A maximum likelihood approach would minimize the global misfit ϕ:

$$\min_{\mathbf{m}} \phi(\mathbf{m}) = \frac{1}{2}(F(\mathbf{m}) - \mathbf{d})^\top \boldsymbol{\Sigma}_d^{-1}(F(\mathbf{m}) - \mathbf{d}). \tag{8}$$

However, this problem is typically ill posed, and there are many possible solutions that minimize the global misfit. To obtain a well-posed problem, two possible routes can be taken. First, if the model $\mathbf{m}$ does not have any particular form, we can assume some smoothness, and this results in a regularized least-squares approach. A second option is when some specific a priori information is available, and we assume that the model $\mathbf{m}$, with n number of cells, can be expressed by a small number of j parameters $\mathbf{p}$. This can be expressed by

$$\mathbf{m} = f(\mathbf{p}), \tag{9}$$

where $f:\mathbb{R}^j \to \mathbb{R}^n$ is a known smooth function that is continuously differentiable.

In some cases, both assumptions about the model are valid. The model can be made of a smooth background and an anomalous body that can be parametrized. That is, we can write

$$\mathbf{m} = \mathbf{m}_s + f(\mathbf{p}), \tag{10}$$

where $\mathbf{m}_s$ is some smooth background and $f(\mathbf{p})$ describes an anomalous conductive or resistive body. This leads to the following regularized problem to be solved:

$$\min_{\mathbf{m}_s,\mathbf{p}} \phi(\mathbf{m}_s, \mathbf{p}) = \frac{1}{2}(F(\mathbf{m}_s + f(\mathbf{p})) - \mathbf{d})^{\top} \times \mathbf{\Sigma}_d^{-1}(F(\mathbf{m}_s + f(\mathbf{p})) - \mathbf{d}) + \beta \mathbf{R}(\mathbf{m}_s). \tag{11}$$

Here, $\mathbf{R}(\cdot)$ is a regularization term that enforces smoothness on the background model and β is a regularization parameter. Additional restrictions, such as bounds on $\mathbf{p}$ or $\mathbf{m}_s$, can also be invoked. Equation 11 is a discrete optimization problem for the smooth background model $\mathbf{m}_s$ and the parameters $\mathbf{p}$. In general, it is nonconvex, and therefore care must be taken to obtain feasible solutions.

We propose a hybrid approach in which we use a block coordinate descent (Gill et al., 1981), to fix $\mathbf{m}_s$ and minimize over $\mathbf{p}$ in the first, or parametric stage, and then we fix $\mathbf{p}$ and minimize over $\mathbf{m}_s$ in the second, or voxel-based stage. Another option is to run the voxel-based stage first prior to the parametric stage, but our experience so far has shown that the former procedure has produced better results. Each stage of our hybrid scheme can be run through once, or it can be iterated if the stopping criteria have not been met. These stopping criteria are when the inversion has either converged to a normalized data misfit of one, has reached a maximum number of user-defined iterations, or when a Gauss-Newton step that lowers the normalized data misfit by 0.1% can no longer be found. The normalized data misfit, hereafter the *data misfit*, is defined as

$$\phi_d = \frac{1}{N}\|\mathbf{W}_d(\mathbf{d}^{\text{obs}} - \mathbf{d}^{\text{pred}})\|_2^2, \tag{12}$$

where N is the number of data, $\mathbf{W_d}$ is a diagonal matrix with the reciprocal of data error standard deviations, $\mathbf{d}^{\text{obs}}$ is a vector of observed data, $\mathbf{d}^{\text{pred}}$ is a vector of predicted data, and $\|\|_2^2$ is the squared ℓ^2-norm. The program may also be terminated if the inversion is deemed to be overfitting the data by placing obvious resistivity artifacts near the transmitter or receiver locations.

This hybrid approach has the advantage of scale separation, in that, the parametric inversion of $f(\mathbf{p})$ typically affects data locally, whereas optimizing over $\mathbf{m}_s$ affects data globally, and it can fit large-scale and smooth features. In the first parametric stage, our method searches for one anomaly of interest, either conductive or resistive, in a background $\mathbf{m}_s$. This background can either be a uniform half-space or a heterogeneous resistivity distribution from a priori information or previous inversion work. Once again, we solve time-dependent quasi-static Maxwell's equations, with initial and boundary conditions as shown in equations 1 through 5.

Our parametric hybrid approach finds an optimal anomaly in the shape of a skewed Gaussian ellipsoid, by means of a finite-volume discretization on local and global OcTree meshes (Haber and Schwarzbach, 2014). The inversion requires an initial guess, which is composed of the quantities, r_x, r_y, r_z, ϕ_x, ϕ_y, ϕ_z, x_0, y_0, z_0, ρ_0, and ρ_1. The values r and ϕ represent an estimate for the radius and rotation angle of the ellipsoid for each Cartesian direction, whereas x_0, y_0, and z_0 represent the center coordinates of the anomaly, and ρ_0 and ρ_1 are the background and anomalous resistivities. These resistivity values can be fixed by the user, or alternatively, the optimal resistivity can be set as a parameter in the inversion. The initial guesses for radii and rotation angles are multiplied together to give a resulting matrix $\mathbf{T}$ as shown in equations 13–17. Equation 18 then forms a symmetric positive definite matrix $\mathbf{M}$, composed of stretching and skewing parameters m_1 through m_6: More information regarding rotation matrices can be found in Modersitzki (2003). All unscaled parameters $\tilde{\mathbf{p}}$ are scaled by elementwise division denoted by $\oslash$ with the vector $\mathbf{s}$, to improve the conditioning of the system as seen in equations 19 and 20. The vector $\mathbf{s}$ is composed of an appropriate length scale L, and a characteristic resistivity $\hat{\rho}$. In total, $\mathbf{p}$ contains 11 scaled parameters that are used in the parametric inversion:

$$\mathbf{S} = \begin{pmatrix} \frac{1}{r_x} & 0 & 0 \\ 0 & \frac{1}{r_y} & 0 \\ 0 & 0 & \frac{1}{r_z} \end{pmatrix}, \tag{13}$$

$$\mathbf{R}_x = \begin{pmatrix} 1 & 0 & 0 \\ 0 & \cos(\phi_x) & -\sin(\phi_x) \\ 0 & \sin(\phi_x) & \cos(\phi_x) \end{pmatrix}, \tag{14}$$

$$\mathbf{R}_y = \begin{pmatrix} \cos(\phi_y) & 0 & \sin(\phi_y) \\ 0 & 1 & 0 \\ -\sin(\phi_y) & 0 & \cos(\phi_y) \end{pmatrix}, \tag{15}$$

$$\mathbf{R}_z = \begin{pmatrix} \cos(\phi_z) & -\sin(\phi_z) & 0 \\ \sin(\phi_z) & \cos(\phi_z) & 0 \\ 0 & 0 & 1 \end{pmatrix}, \tag{16}$$

$$\mathbf{T} = \mathbf{S}\mathbf{R_x}\mathbf{R_y}\mathbf{R_z}, \tag{17}$$

$$\mathbf{M} = \begin{pmatrix} m_1 & m_4 & m_5 \\ m_4 & m_2 & m_6 \\ m_5 & m_6 & m_3 \end{pmatrix} = \mathbf{T}^{\mathrm{T}}\mathbf{T}, \tag{18}$$

$$\tilde{\mathbf{p}} = \begin{pmatrix} m_1 \\ m_2 \\ m_3 \\ m_4 \\ m_5 \\ m_6 \\ x_0 \\ y_0 \\ z_0 \\ \log(\rho_0) \\ \log(\rho_1) \end{pmatrix} \mathbf{s} = \begin{pmatrix} L^{-2} \\ L^{-2} \\ L^{-2} \\ L^{-2} \\ L^{-2} \\ L^{-2} \\ L \\ L \\ L \\ \log(\hat{\rho}) \\ \log(\hat{\rho}) \end{pmatrix}, \tag{19}$$

$$\mathbf{p} = \tilde{\mathbf{p}} \oslash \mathbf{s}. \tag{20}$$

For any position, x, y, z in our spatial domain Ω, we define

$$\mathbf{x} = \begin{pmatrix} x \\ y \\ z \end{pmatrix} \quad \mathbf{x_0} = \begin{pmatrix} x_0 \\ y_0 \\ z_0 \end{pmatrix}, \tag{21}$$

and we introduce the level set function τ in each mesh cell

$$\tau = c - (\mathbf{x} - \mathbf{x_0})^{\mathbf{T}} \mathbf{M} (\mathbf{x} - \mathbf{x_0}), \tag{22}$$

where c represents a positive constant. We use τ, ρ_0, and ρ_1 to generate the resistivity distribution through an analytic step function

$$\rho(\tau, \rho_0, \rho_1) = \rho_0 + \frac{1}{2}(1 + \tanh(a\tau))(\rho_1 - \rho_0), \tag{23}$$

where $\lim_{\tau \to -\infty} \rho(\tau, \rho_0, \rho_1) = \rho_0$, $\lim_{\tau \to +\infty} \rho(\tau, \rho_0, \rho_1) = \rho_1$, and $\rho(\tau = 0, \rho_0, \rho_1) = 1/2\,(\rho_0 + \rho_1)$.

We choose to use a hyperbolic tangent for the analytic step function, but other choices are possible (Tai and Chan, 2004). The transition zone between ρ_0 and ρ_1 occurs when $\tau = 0$, also known as the *zero level set* (Osher and Sethian, 1988), and its width is controlled by the parameter a. The optimization of the inversion follows a conventional Gauss-Newton procedure for time-domain AEM data (Haber and Schwarzbach, 2014), and a line search is used to determine an appropriate step length within a minimum and maximum value. The calculation of the parametric sensitivity matrix $\mathbf{J}$ is discussed further in Appendix A. In case we want to invert only for $\mathbf{m} = f(\mathbf{p})$, the parametric code can be used as a stand-alone algorithm, where $\mathbf{m}_s$ is fixed. Otherwise, the hybrid technique is achieved by setting the parametric inversion model as the initial and reference model when optimizing over $\mathbf{m}_s$, and iterating back to the parametric stage if the target data misfit has not been reached.

RESULTS

Synthetic dipping plate

To test our inversion, we built a synthetic model representing a typical mineral exploration scenario in which a narrow target exists with a large resistivity contrast: a thin, buried, dipping conductive platelike body in a resistive background. For simplicity, no topographic relief is included in this example. Figure 1a–1c portrays sections through the synthetic model in each Cartesian direction. In the case in which a portion of the optimal ellipsoid resides above the ground, we set this region to a typical resistivity value for air. A time-domain AEM survey is simulated at a height of 37.5 m above the ground with 49 transmitter locations over the dipping plate as shown by stars in Figure 1a. The data are composed of z-component $\frac{d\mathbf{B}}{dt}$ data at 19 time channels ranging from 10 to 7000 μs contaminated with 5% Gaussian noise. The model is discretized on an OcTree mesh with core cells of $20 \times 20 \times 20$ m, and the resistivity of the plate is 3 Ωm in a uniform 3000 Ωm background. The dimensions of the dipping plate are $320 \times 60 \times 640$ m in x, y, z, respectively, with a near-vertical dip of 80° in the positive y-direction (east). Figure 1d–1f shows the results from a voxel-based inversion alone (Haber and Schwarzbach, 2014), which demonstrates how this type of algorithm has trouble imaging sharp boundaries, such as a thin, dipping plate. The resulting anomaly gets smeared, the resistivity magnitude is much too high, and the inversion is unable to capture the true dip.

For the parametric inversion, the initial guess consists of a 50-m-radius sphere located at $[x, y, z] = [-120, 0, -150]$ in a uniform background. This is the same initial guess as the voxel-based inversion. In the first example, we assume that we know the true anomalous and background resistivity, and in the second trial, we assign incorrect values and let the inversion determine the optimal parameters. Having a sphere as a starting guess provides minimal information with regard to the true size and dip of the anomaly, and we believe it is a reasonable estimate without having any a priori knowledge. Based on experience with the code, we set the adjustable inversion parameters from equations 19, 22, and 23 to $L = 100$, $\tilde{\rho} = 10$, $a = 10$ and $c = 0.7$, and more information about these parameters can be found in Appendix A.

When we fix the anomalous and background resistivities to the true values, we finish optimizing over $\mathbf{p}$ in 32 Gauss-Newton iterations. For the parametric stage, only a small number of poorly correlated parameters are sought. As such, a regularization term is not required, and the regularization parameter β is set to zero. In our experience, the lack of regularization has not been an issue, but different regularization schemes in parametric inversions can be found in Dorn and Lesselier (2006), van den Doel and Ascher (2006), and Aghasi et al. (2011). At this point, we proceed to the voxel-based stage to solve for $\mathbf{m}_s$, but in this example, there are no regional background features to resolve, and the sharp resistivity contrast between the homogeneous background and the thin plate favors a parametric inversion. Consequently, when we run the voxel-based stage, the result does not decrease the data misfit without adding spurious inversion artifacts. Although the parametric result does not reach the target data misfit, the voxel-based stage overfits the data, and the model after the first parametric stage is chosen as the final answer. Sections through this model are shown in Figure 1f, 1h, and 1i. These images show that the parametric algorithm is able to accurately recover the size, shape, and dip of the anomaly compared with the true answer. The dip of the parametric model is roughly 74° to the east, and this closely matches the true dip of 80° to the east. One aspect not perfectly detected is the position of the plate bottom, which sits at approximately 600 m in the parametric recovery and 800 m in the true model. This discrepancy can most likely be attributed to reduced sensitivity to model cells at these depths.

We now allow the resistivity to be variable, and we assign incorrect anomalous and background values of 1 and 1000 Ωm. We are free to choose any combination of two resistivities for the starting guess, but naturally, the further the starting guesses are from the true resistivities, the more difficulties the program will have converging to the correct solution. With our starting guesses, the parametric stage concludes after 29 Gauss-Newton iterations. As before, the voxel-based stage adds little improvement, and the model after the parametric stage is chosen as the final result. Cross sections through the recovered variable resistivity inversion are displayed in Figure 1j–1l. The inversion defines the shape of the target with accurate precision with an estimated dip of 73° to the east. The depth extent of the anomaly is slightly closer to the true model compared with the case when the true resistivities are assigned. Recovered anomalous and background resistivities are 3.97 and 3173 Ωm, respectively.

A plan map of observed and predicted data at a midrange time channel, 1110 μs, is displayed in Figure 2a and 2b. The plot is for the fixed resistivity inversion, where the true values are assigned,

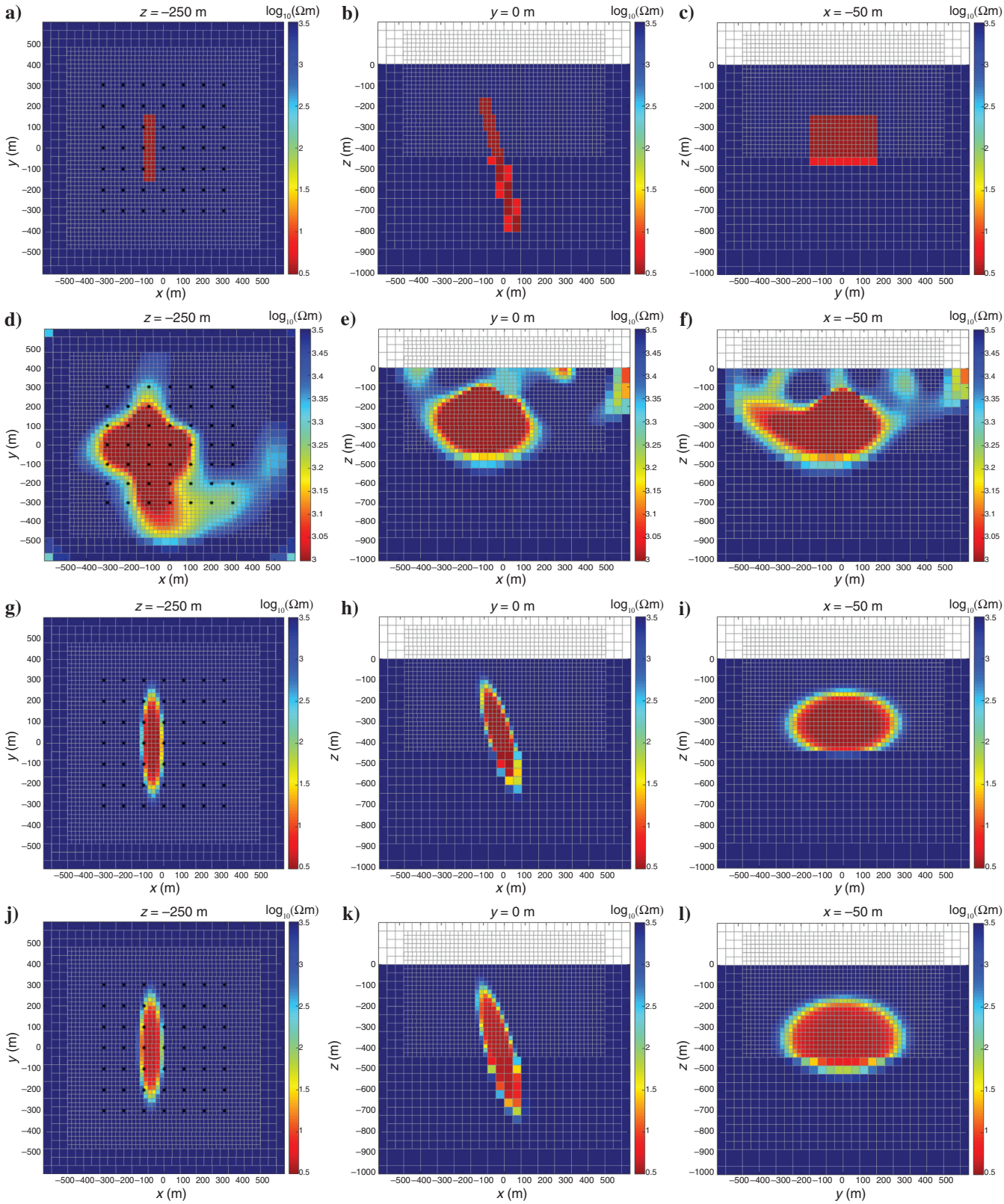

Figure 1. Plan view depth slices and cross sections through the true model, recovered voxel-based inversion only and recovered parametric models. (a) True model at $z = -250$ m. (b) True model along $y = 0$ m. (c) True model along $x = -50$ m. (d) Voxel model at $z = -250$ m. (e) Voxel model along $y = 0$ m. (f) Voxel model along $x = -50$ m. (g) Parametric model at $z = -250$ m for fixed ρ. (h) Parametric model along $y = 0$ m for fixed ρ. (i) Parametric model along $x = -50$ m for fixed ρ. (j) Parametric model at $z = -250$ m for variable ρ. (k) Parametric model along $y = 0$ m for variable ρ. (l) Parametric model along $x = -50$ m for variable ρ.

although predicted data are similar in the variable resistivity case. An observed and predicted sounding from a selected location, marked with a cross in Figure 2a, is plotted in Figure 2c. Collectively, these images demonstrate the high level of agreement between the observed and predicted data. The initial and final data misfits are 70.4 and 3.8 for the fixed-resistivity case and 2328.4 and 2.8 for the variable-resistivity scenario. For both trials, the misfit at each Gauss-Newton iteration is summarized in Figure 2d. The misfit summary shows that both parametric inversions make excellent strides in reducing the data misfit toward optimal recovery, where the data misfit is equal to one.

A possible explanation for the lower misfit when using a variable resistivity is that a skewed Gaussian ellipsoid cannot perfectly recover the staircase nature of a discretized dipping plate. It is also worth remembering that within the transition zone between ρ_0 and ρ_1, the anomaly will not contain the true resistivity value, but instead a weighted average of ρ_0 and ρ_1. Therefore, if the anomalous resistivity quantity is allowed to vary, it is possible that the inversion can find a shape and resistivity combination that fits the observed data better than having prescribed the true values of ρ_0 and ρ_1. This arises because there are more degrees of freedom in representing the earth model, and the Gaussian parametric model with slightly smoothed interfaces cannot exactly represent a plate. As an additional check for the fixed-resistivity algorithm, the data misfit decreases to the same value of 2.8 with an equivalent shape as the variable option when using fixed resistivities of $\rho_0 = 3.97$ Ωm and $\rho_1 = 3173$ Ωm.

Furthermore, from trials not shown in the paper, the exact location and shape of the initial guess do not significantly affect the inversion result, and therefore reasonable estimates of the anomaly

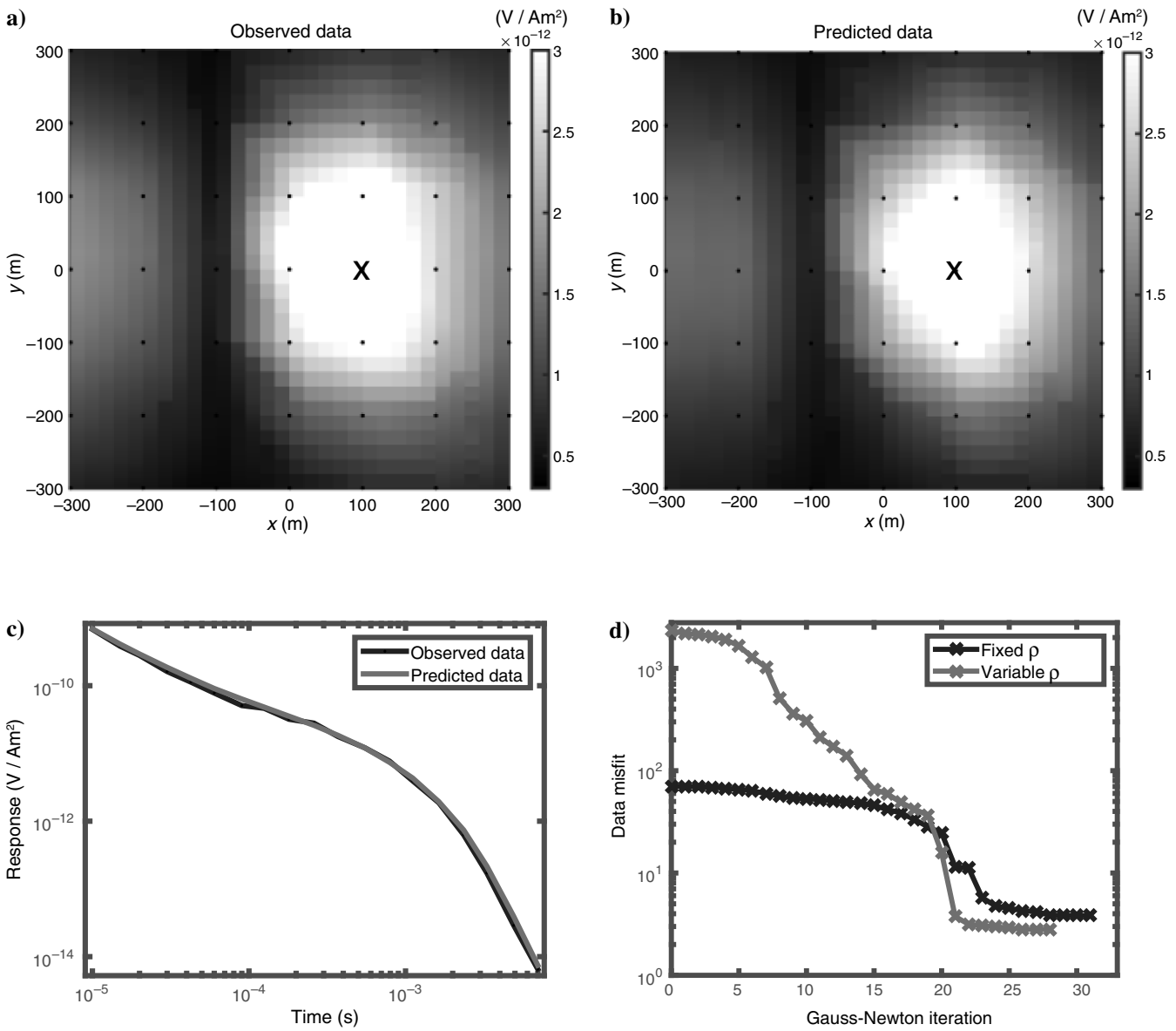

Figure 2. Synthetic dipping plate observed and predicted z-component $\frac{d\mathbf{B}}{dt}$ data. (a) Observed data at 1110 μs for fixed ρ, with a selected sounding marked with a cross. (b) Predicted data at 1110 μs for fixed ρ, with a selected sounding marked with a cross. (c) Fixed ρ observed and predicted data at selected sounding location. (d) Fixed and variable resistivity data misfit progression.

from different users should produce comparable models. Also, based on additional testing, the parametric inversion can deliver good results when dealing with smaller resistivity contrasts than the three-order-of-magnitude difference between the target and background shown in our synthetic example. In general, the encouraging results from the synthetic dipping plate parametric inversion lead us to believe that similar success can be found with a more complicated field example.

Caber volcanogenic massive sulfide deposit

The parametric hybrid approach is now applied to data from the Caber VMS deposit of western Quebec, Canada, as shown in Figure 3a. Within the Superior Province, the copper- and zinc-rich Caber deposit is part of the Matagami camp of the Abitibi Greenstone Belt (Carr et al., 2008). Geologically, the prominent McIvor fault separates Caber and accompanying gabbros, rhyolites, and basalts from a granodiorite unit to the northeast (Adair, 2011). The local geology in plan view is depicted in Figure 3a, and a simplified cross section is displayed in Figure 3b (Prikhodko et al., 2010). The cross section shows there is a thin conductive overburden layer above the ore body that thickens to the northeast. The deposit itself is cigarlike in shape with a steep dip of 75°–85° to the southwest and a strike direction of 125° (Adair, 2011). The cross section also shows the near-vertical nature of a narrow shear zone proximal to the deposit and nearby steeply dipping rhyolite and gabbro units.

The thin, buried nature of the Caber deposit, coupled with its position below conductive overburden, makes it a challenging target to detect with AEM techniques. Fortunately, the elevated conductivity of the deposit compared with surrounding rock units produces an anomalous electromagnetic response that is measurable from the air (Prikhodko et al., 2010). A small shear zone next to the deposit, which may be more conductive relative to the background but more resistive than the deposit, may contribute to the conductive response. For the purpose of this paper, the response from the deposit and any contribution from the shear zone will be considered the target of interest.

Caber inversion results

The Caber AEM field data are inverted with our parametric hybrid approach. The AEM data at Caber consist of eight lines of versatile time-domain electromagnetic (VTEM-35) data, collected in 2012 with a 35-m-diameter transmitter loop and a peak dipole moment of 1,300,000 Am^2. See Allard (2007) for a review of VTEM and other AEM systems. The flight lines are spaced 50 m apart with a heading of 225°.

For the parametric stage of our inversion, a subsection of the total AEM survey over the Caber deposit is used, consisting of 102 transmitters of z-component $\frac{d\mathbf{B}}{dt}$ data with 11 time channels ranging from 505 to 2021 μs. The model is discretized on an OcTree mesh with core cells of $20 \times 20 \times 20$ m. The initial guess is a 50-m-radius sphere, buried 150 m below the surface, with resistivity of 0.2 Ωm positioned in the center of the recorded anomaly with a background of 1000 Ωm. In this field example, the true anomalous and background quantities are unknown, and ρ_0 and ρ_1 are variables solved for in the inversion. Data uncertainties of 5% plus a time-channel-dependent noise floor are applied. The noise floor is set to one order of magnitude lower than a 1000 Ωm half-space response. This varying noise floor is selected to weight each time channel as equally as possible in the inversion. The optimization over $\mathbf{p}$ concludes after 30 Gauss-Newton iterations, and the sections through the initial guess and the resulting model in each Cartesian direction are shown in Figure 4a through 4f. The recovered model has a steep 80° dip to the southwest, which agrees with the known dip of the deposit. The final resistivities of the anomaly and background are 0.084 and 2118 Ωm, respectively. As in the synthetic case, similar results are produced if the initial guess is moved to various locations and depths near the center of the observed z-component $\frac{d\mathbf{B}}{dt}$ anomaly. The achieved anomaly value of 0.084 Ωm is well within the range of resistivities for massive sulfides (Palacky, 1988), and it is similar to the value of 0.14 Ωm over a 30-m thickness obtained by Maxwell plate modeling (EMIT, 2005) of the 2012 AEM data over Caber from previous work (Prikhodko et al., 2012).

A plan map of the observed and predicted data for a midrange time channel, 1010 μs, is displayed in Figure 5a and 5b. Overall, there is close agreement between the observed and predicted data, as they both exhibit a similar asymmetric double-peaked response, indicative of a single-dipping plate anomaly. Some discrepancies between the data sets exist, such as the break in the observed data that separates the southern lobe of the double peak that is not present in the predicted data. The inability to resolve fine levels of detail, such as this break, is a limitation of the first parametric stage of the hybrid approach, but the primary purpose of finding a best-fitting skewed Gaussian ellipsoid that matches the overall trend of the data is achieved. Observed and predicted data at a selected sounding in the center of the northern lobe, marked with a cross in Figure 5b are shown in Figure 5c, and a strong agreement is evident. The initial and final data misfits are 58.6 and 5.7, respectively, and the data misfit progression is summarized in Figure 5d. Once again, the parametric approach reduces the data misfit by over an order of magnitude.

For the second stage of the hybrid approach, we place the parametric result as the initial and reference model and we optimize over

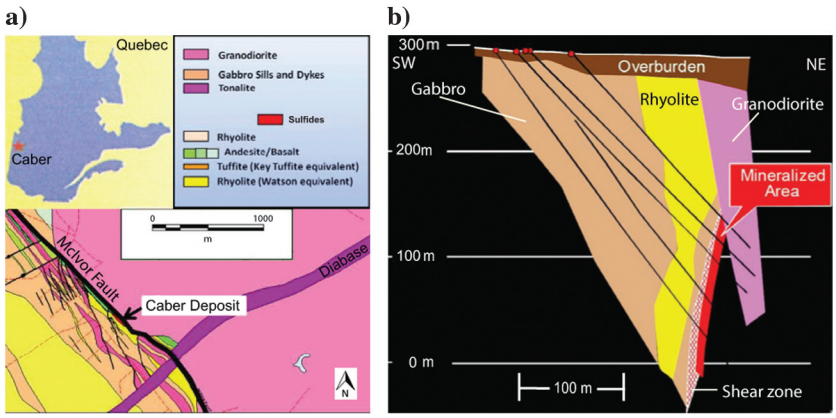

Figure 3. (a) Caber deposit location and geology, modified from Prikhodko et al. (2010) and Adair (2011). (b) Simplified deposit cross section with drilling traces.

$\mathbf{m}_s$, allowing the resistivity in each mesh cell to vary. Data from 19 time channels ranging from 167 to 2021 μs are included, and responses below a threshold of $1e-13\frac{V}{Am^2}$ are discarded because of potential noise concerns. In total, 727 transmitter locations from across the entire survey area are inverted with the same error assignments as in the parametric stage. Data over the central anomaly are included to allow the resistivity and shape of the parametric result to adjust if needed.

We optimize over $\mathbf{m}_s$ in nine Gauss-Newton iterations and converge to a normalized data misfit of 0.95. Figure 4g–4i shows sections through the final hybrid parametric model. Once again, the thin conductor is imaged, representing the Caber deposit. A different colorbar is used for the hybrid result to show the weakly conductive overburden and the strongly conductive target together. The Caber anomaly steeply dips to the southwest with a dip of 80°, and an overburden unit over the conductor initially thickens to the northeast. The recovered size, dip, and presence of the overburden corroborates geologic information from Figure 3b, which adds confidence to this hybrid result. The shape and sharp boundaries of the dipping conductor are achieved through the parametric inversion, whereas the voxel-based inversion adds smooth features, such as the overburden. Although the voxel-based stage can alter the shape and resistivity of the Caber deposit, we notice that the anomaly only changes slightly from its state following the parametric stage. We do not believe this will occur in all examples, but the distinct nature of the small low-resistivity anomaly, coupled with the smooth regional

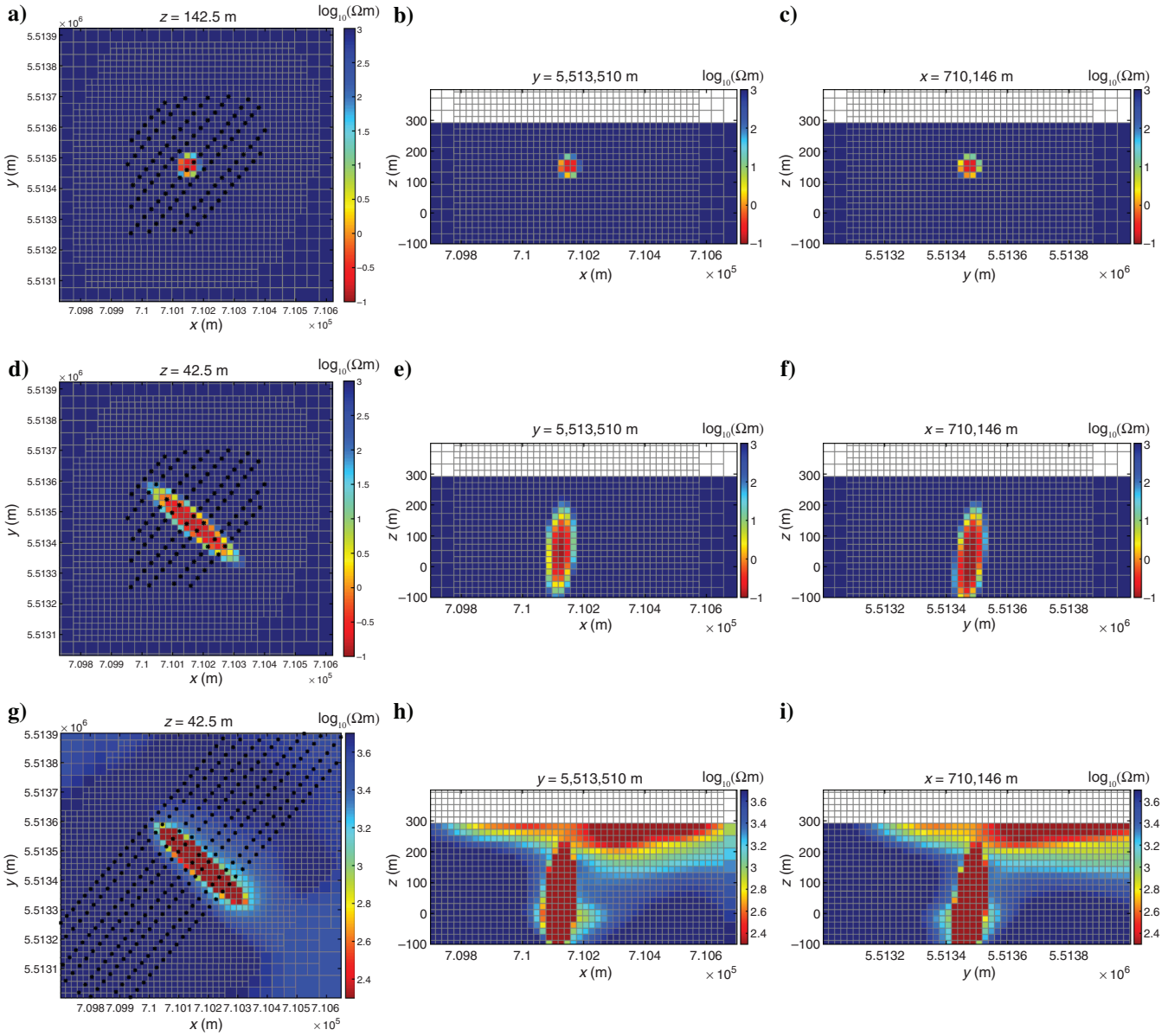

Figure 4. Plan view depth slices and cross sections through the initial guess and recovered Caber parametric and hybrid models. (a) Initial guess at $z = 142.5$ m. (b) Initial guess along $y = 5{,}513{,}510$ m. (c) Initial guess along $x = 710{,}146$ m. (d) Parametric model at $z = 42.5$ m. (e) Parametric model along $y = 5{,}513{,}510$ m. (f) Parametric model along $x = 710{,}146$ m. (g) Hybrid model at $z = 42.5$ m. (h) Hybrid model along $y = 5{,}513{,}510$ m. (i) Hybrid model along $x = 710{,}146$ m.

overburden and nearly homogeneous background at Caber allows for our hybrid inversion to converge with only one combined iteration of the parametric and voxel-based stages.

Observed and predicted z-component $\frac{d\mathbf{B}}{dt}$ data from time channel 505 μs, are illustrated in Figure 6. The predicted data at this time channel closely resemble the observed data, and they clearly illustrate the response of the Caber deposit in addition to the conductive overburden in the northeast portion of the survey area. Holes in the observed and predicted data represent areas of resistive terrain, where z-component $\frac{d\mathbf{B}}{dt}$ responses drop below $1e-13\,\frac{\mathrm{V}}{\mathrm{Am}^2}$. Data from much of the southwest survey area are not shown due to data below this noise threshold.

To validate and ground truth our field inversion, Figure 7 displays a front and side view of a 0.4 Ωm isosurface from the parametric result in black, the hybrid result in dark gray, the massive sulfide deposit outline from drilling (M. Allard, personal communication, 2014) in light gray, and the aforementioned plate models for individual lines (Prikhodko et al., 2012), in medium gray. The image demonstrates how the depiction of the Caber anomaly is extremely similar after the parametric and hybrid stages; however, the hybrid result is treated as the final model. The hybrid isosurface accurately portrays the general size and dip of the target anomaly, although it stretches further to the southeast compared with the deposit model. Interestingly, previous AEM plate modeling also placed conductive plates extending off the deposit. This suggests that additional conductive material to the southeast of the recorded sulfide zone is needed to explain the observed response. This anomalous material outside the deposit could be due to an unknown extension of the economic mineralization or the mapped shear zone shown in Figure 3b, or some combination of the two. This demonstrates how the parametric hybrid inversion provides a new interpretation to the cause of the conductive response from the 2012 time-domain AEM data.

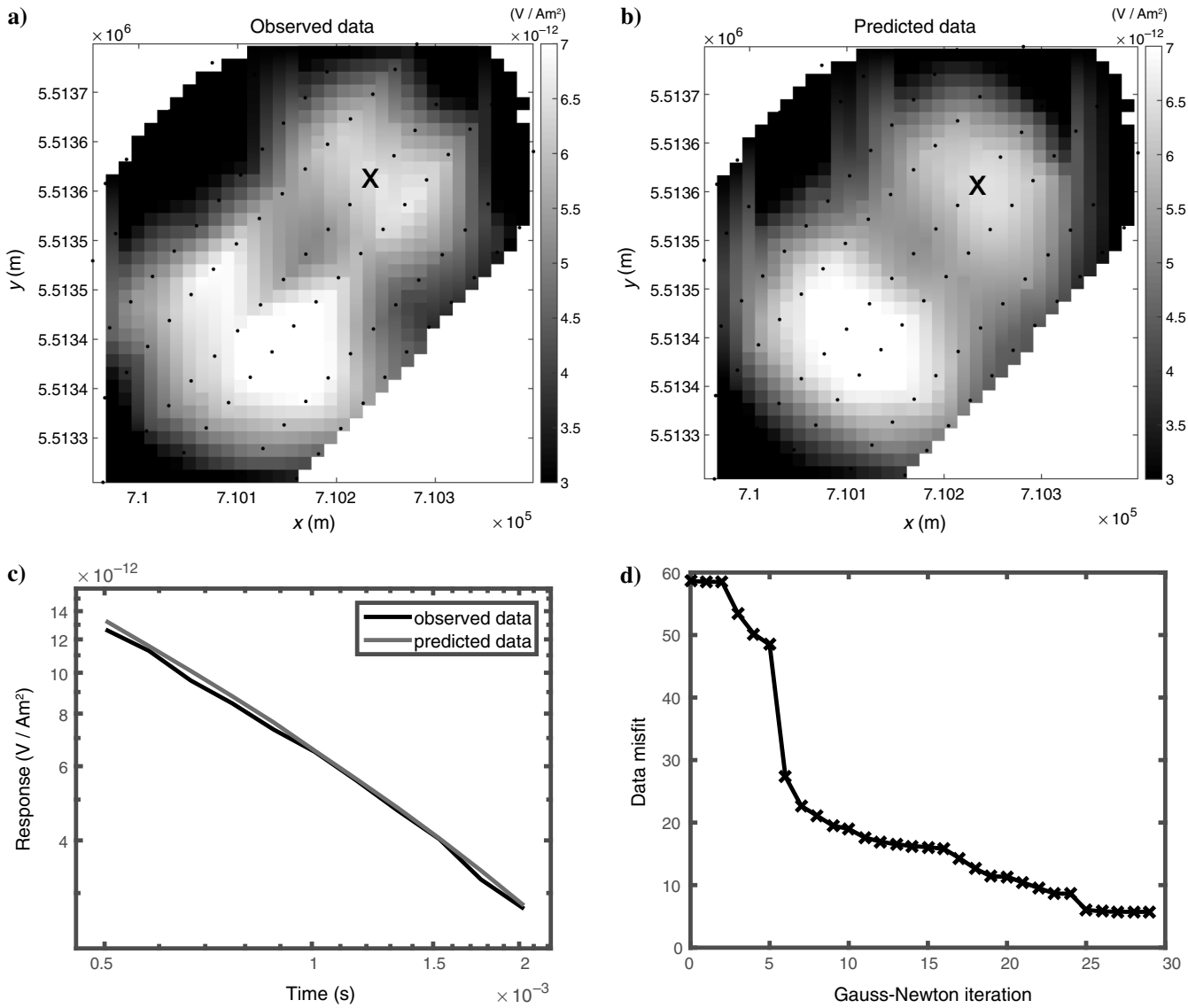

Figure 5. Caber observed and predicted z-component $\frac{d\mathbf{B}}{dt}$ data. (a) Observed data at 1010 μs with a selected sounding marked with a cross. (b) Predicted data at 1010 μs with a selected sounding marked with a cross. (c) Observed and predicted data at selected sounding location. (d) Data misfit progression.

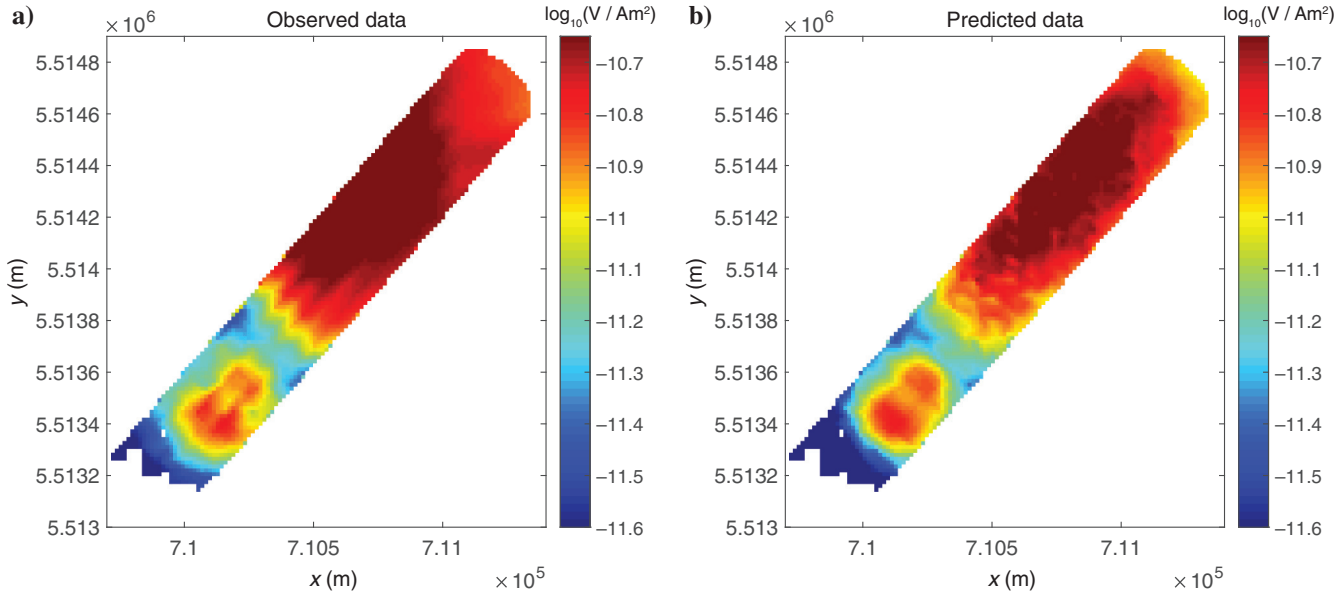

Figure 6. Caber observed and predicted data at 505 μs from the parametric hybrid inversion. (a) Observed data. (b) Predicted data.

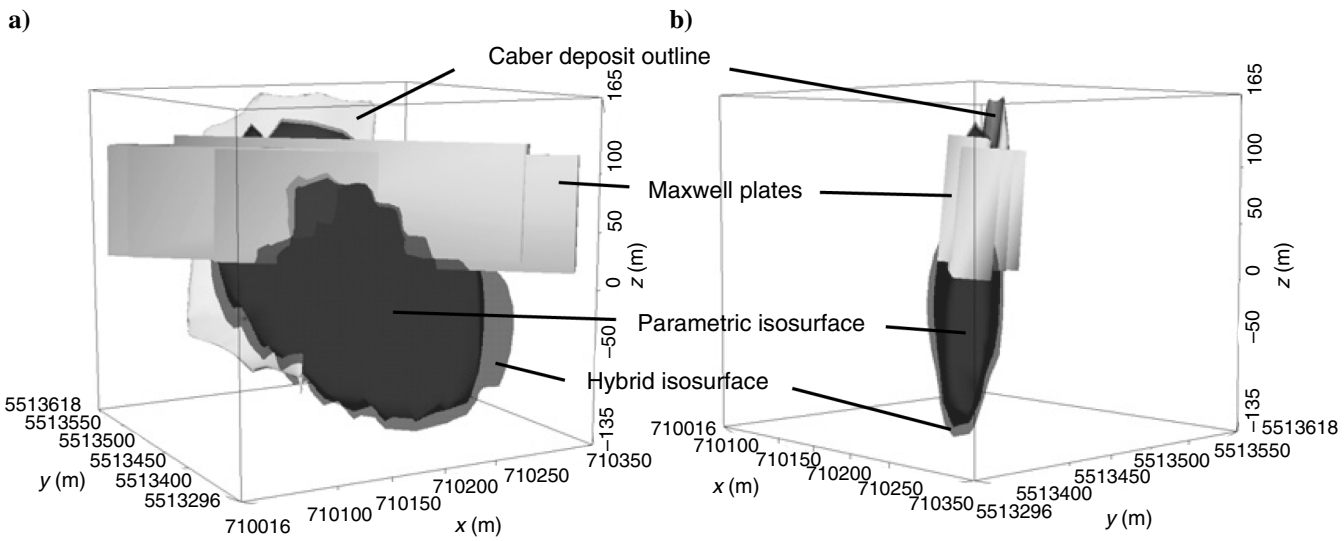

Figure 7. Caber deposit outline with inversion results. The 0.4 Ωm isosurface (filled black) from the parametric stage, and 0.4 Ωm isosurface (dark gray) from hybrid inversion overlaid on Caber massive sulfide deposit model from drilling (single light gray outline) and Maxwell plate anomalies (multiple medium gray sheets) from five central lines of AEM data (Prikhodko et al., 2012). (a) Looking northeast. (b) Looking northwest.

DISCUSSION

A parametric hybrid inversion has been developed for time-domain AEM data to recover a target represented by a skewed Gaussian ellipsoid in a smooth background. Our approach is tested on a synthetic and a field scenario, where the target is a thin, narrow, conductive, platelike body with a large resistivity contrast between itself and the resistive background. Both examples recover models that agree well with either the true synthetic answer or geologic information from past drilling, respectively. The approach can be used as an alternative to a purely voxel-based inversion, where sharp boundaries and large resistivity contrasts may not be imaged accurately. The parametric hybrid models are produced using a basic initial guess of a sphere without a priori information, which adds robustness to the algorithm. The results show that our parametrization is well suited for a thin, dipping plate target, and we believe this approach should also work in other exploration environments in which a skewed Gaussian ellipsoid might be applicable, such as mapping large intrusions or kimberlites.

CONCLUSION

We acknowledge that more complex scenarios need to be explored to fully demonstrate the effectiveness of our algorithm. In our synthetic case, the parametric stage recovers the dipping plate accurately and the voxel-based stage does not provide additional improvements. Furthermore, in the Caber example, the hybrid inversion is able to converge in only one parametric and voxel-based

stage. Therefore, to thoroughly test the algorithm, future examples will look at models with a more detailed background and a smaller resistivity contrast compared with the primary target, where further iterations between the parametric and voxel-based stages are needed. In this manner, the algorithm will be tested in a scenario in which a mixture of galvanic and vortex currents flow through and within the target, respectively. These examples will be addressed in a future publication.

We also point out that in this incipient version of the code, only one anomaly of interest is produced in the parametric stage, and as a result due care must be taken when running the inversion. In a scenario in which two nearby conductive or resistive anomalies exist, the response may be modeled erroneously as a single anomaly. Future generations of the code will explore parametric inversions with multiple anomalies and a variety of regularization schemes. In the meantime, a careful analysis of the observed and predicted data is needed to see whether one or multiple bodies are warranted. In this example, a priori information from plate modeling and drilling suggested that the Caber deposit could be depicted appropriately as one anomaly. Finally, we have used only z-component $\frac{d\mathbf{B}}{dt}$ data in this research, but one could additionally use x- or y-components $\frac{d\mathbf{B}}{dt}$ data or **B**-field measurements.

ACKNOWLEDGMENTS

The authors would like to thank Geotech, Ltd., for providing the AEM data over the Caber deposit, to M. Allard from Glencore for providing the Caber geologic model, and to all members of the University of British Columbia Geophysical Inversion Facility for their suggestions and ideas. We also acknowledge and thank the Natural Sciences and Engineering Research Council of Canada for help in funding this research.

APPENDIX A

PARAMETRIC SENSITIVITY AND INITIAL PARAMETER SELECTION

The Gauss-Newton optimization to minimize equation 11 requires a sensitivity matrix $\mathbf{J}_{i,j}$, or $\frac{\partial d_i}{\partial p_j}$, where d_i is the ith data point and p_j is the jth inversion parameter. For p_1 through p_9, we use the chain rule to calculate $\mathbf{J}_{i,j}$ as shown in equation A-1:

$$\mathbf{J}_{i,j} = \sum_{\alpha,\beta} \frac{\partial d_i}{\partial \rho_\alpha} \frac{\partial \rho_\alpha}{\partial \rho_\beta} \frac{\partial \rho_\beta}{\partial \tau} \frac{\partial \tau}{\partial \tilde{p}_j} \frac{\partial \tilde{p}_j}{\partial p_j}, \tag{A-1}$$

where ρ_α is the cell center resistivity for each local mesh cell, α is the local mesh cell index, ρ_β is the cell center resistivity for each global mesh cell, and β is the global mesh cell index. This mesh domain separation into local and global meshes is used for maximum computational efficiency as described in Haber and Schwarzbach (2014). For p_{10}, and similarly for p_{11}, $\mathbf{J}_{i,j}$ is shown in equation A-2, where the derivative with respect to τ is replaced with a derivative with respect to the initial resistivity ρ_0 or ρ_1:

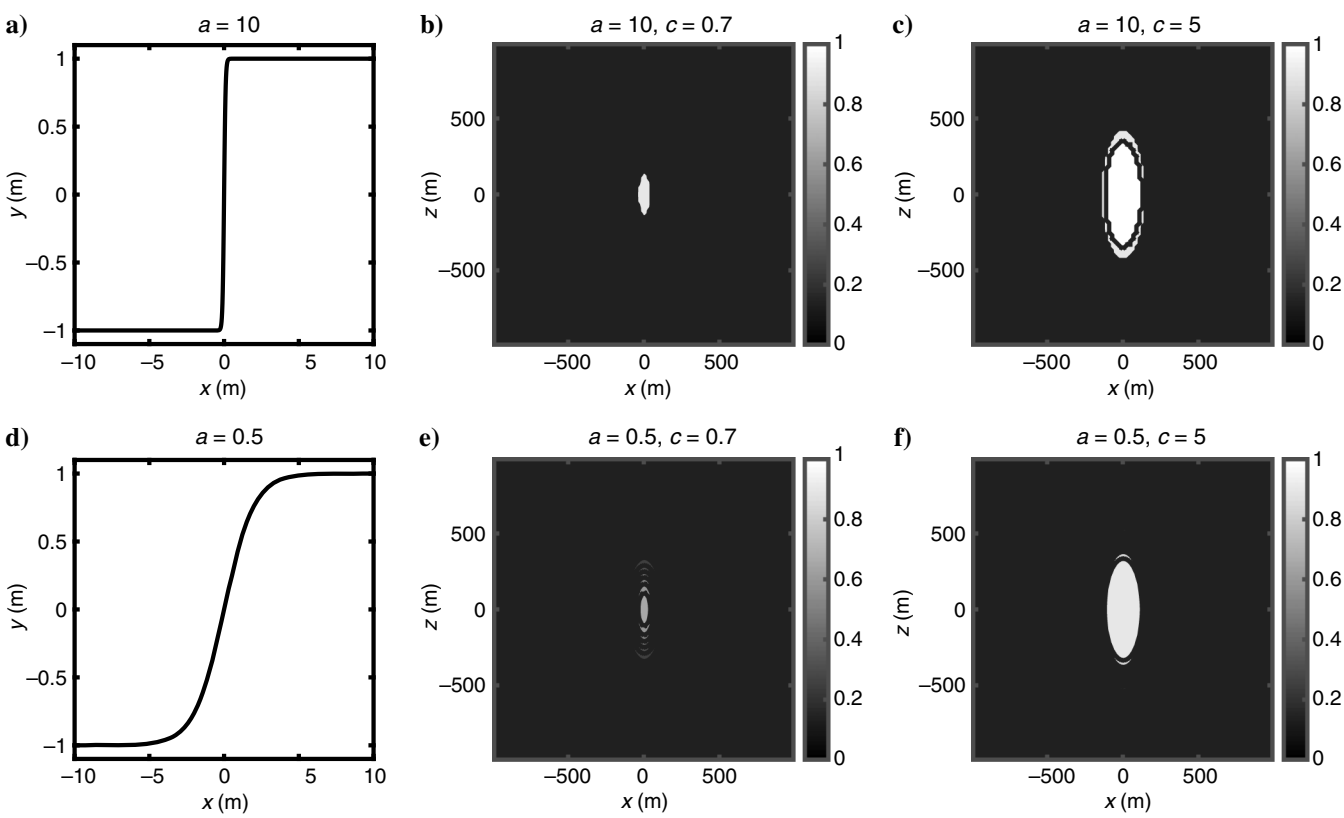

Figure A-1. (a) Analytic step function with $a = 10$. (b) Gaussian ellipsoid parametrization with $a = 10$ and $c = 0.7$. (c) Gaussian ellipsoid parametrization with $a = 10$ and $c = 5$. (d) Analytic step function with $a = 0.5$. (e) Gaussian ellipsoid parametrization with $a = 0.5$ and $c = 0.7$. (f) Gaussian ellipsoid parametrization with $a = 0.5$ and $c = 5$.

$$\mathbf{J}_{i,j} = \sum_{\alpha,\beta} \frac{\partial d_i}{\partial \rho_\alpha} \frac{\partial \rho_\alpha}{\partial \rho_\beta} \frac{\partial \rho_\beta}{\partial \rho_0} \frac{\partial \rho_0}{\partial \tilde{p}_j} \frac{\partial \tilde{p}_j}{\partial p_j}. \tag{A-2}$$

Prior to calculating $\mathbf{J}_{i,j}$, the user-defined inversion parameters $L, \tilde{\rho}, a, c,$, from equations 19, 22, and 23 need to be chosen. We suggest choosing L, such that it represents a typical length scale of the problem, meaning it should be no smaller than a minimum mesh cell size and no larger than the biggest length scale of the anomaly of interest. Select $\tilde{\rho}$, such that it represents a moderately low resistivity value in the inversion. With resistivities varying by many orders of magnitude, this can be difficult to select, but we have chosen 10 Ωm for the synthetic and field example. Based on initial tests, the choice of L or $\tilde{\rho}$ does not substantially change the inversion results, but it mostly helps to stabilize the Gauss-Newton system.

The parameters a and c collectively change the width of the transition zone between ρ_1 and ρ_0, as depicted in Figure A-1 with initial parameters $[r_x, r_y, r_z] = [25, 50, 25]$, $[\phi_x, \phi_y, \phi_z] = [0, 0, 0]$, $[x_0, y_0, z_0] = [0, 0, 0]$, and $[\rho_0, \rho_1] = [0, 1]$. Selecting the parameter a to be larger results in a smaller transition zone. Based on our experience, a values larger than 20 can be problematic as the parametric inversion has difficulties finding a suitable Gauss-Newton step. Therefore, we have chosen $a = 10$ for our inversions, and we suggest choosing a value of a between five and 15 for best results. The inversion is less sensitive to the parameter c, and we have chosen $c = 0.7$, although almost identical results occur with $c = 0.5$ to 1.5. Figure A-1a–A-1c demonstrates a sharp step-off function and the resulting ellipsoids with $a = 10$ and the parameter c equal to 0.7 and 5.0, respectively. Figure A-1d–A-1f shows a gradual step-off and the corresponding ellipsoids with $a = 0.5$ and the parameter c set to 0.7 and 5.0, respectively. Figure A-1b displays the ellipsoid anomaly constructed with our suggested choice of inversion parameters.

REFERENCES

Adair, R., 2011, Technical report on the resource calculation for the Matagami project, Quebec: Technical report.

Aghasi, A., M. Kilmer, and E. L. Miller, 2011, Parametric level set methods for inverse problems: SIAM Journal on Imaging Sciences, **4**, 618–650, doi: 10.1137/100800208.

Allard, M., 2007, On the origin of the HTEM species, *in* B. Milkereit, ed., Proceedings of Exploration 07: Fifth Decennial International Conference on Mineral Exploration, Decennial Mineral Exploration Conferences, 353–374.

Carr, P. M., L. M. Cathles, III, and C. T. Barrie, 2008, On the size and spacing of volcanogenic massive sulfide deposits within a district with application to the Matagami district, Quebec: Economic Geology, **103**, 1395–1409, doi: 10.2113/gsecongeo.103.7.1395.

Commer, M., and G. A. Newman, 2004, A parallel finite-difference approach for 3D transient electromagnetic modeling with galvanic sources: Geophysics, **69**, 1192–1202, doi: 10.1190/1.1801936.

Cox, L. H., G. A. Wilson, and M. S. Zhdanov, 2010, 3D inversion of airborne electromagnetic data using a moving footprint: Exploration Geophysics, **41**, 250–259, doi: 10.1071/EG10003.

Cox, L. H., G. A. Wilson, and M. S. Zhdanov, 2012, 3D inversion of airborne electromagnetic data: Geophysics, **77**, no. 4, WB59–WB69, doi: 10.1190/geo2011-0370.1.

Dorn, O., and D. Lesselier, 2006, Level set methods for inverse scattering: Inverse Problems, **22**, R67–R131, doi: 10.1088/0266-5611/22/4/R01.

Dorn, O., E. L. Miller, and C. M. Rappaport, 2000, A shape reconstruction method for electromagnetic tomography using adjoint fields and level sets: Inverse Problems, **16**, 1119–1156, doi: 10.1088/0266-5611/16/5/303.

EMIT, 2005, Maxwell 4.0: Modeling, presentation and visualization of EM and electrical geophysical data: Technical report.

Gill, P. E., W. Murray, and M. H. Wright, 1981, Practical optimization: Academic Press, Inc.

Haber, E., U. M. Ascher, and D. W. Oldenburg, 2004, Inversion of 3D electromagnetic data in frequency and time domain using an inexact all-at-once approach: Geophysics, **69**, 1216–1228, doi: 10.1190/1.1801938.

Haber, E., and S. Heldmann, 2007, An OcTree multigrid method for quasi-static Maxwell's equations with highly discontinuous coefficients: Journal of Computational Physics, **223**, 783–796, doi: 10.1016/j.jcp.2006.10.012.

Haber, E., S. Heldmann, and U. Ascher, 2007a, Adaptive finite volume method for distributed non-smooth parameter identification: Inverse Problems, **23**, 1659–1676, doi: 10.1088/0266-5611/23/4/017.

Haber, E., D. W. Oldenburg, and R. Shekhtman, 2007b, Inversion of time domain three-dimensional electromagnetic data: Geophysical Journal International, **171**, 550–564, doi: 10.1111/j.1365-246X.2007.03365.x.

Haber, E., and C. Schwarzbach, 2014, Parallel inversion of large-scale airborne time-domain electromagnetic data with multiple OcTree meshes: Inverse Problems, **30**, 055011, doi: 10.1088/0266-5611/30/5/055011.

Keller, G. V., 1988, Rock and mineral properties, *in* M. N. Nabighian, ed., Electromagnetic methods in applied geophysics: SEG, 13–52.

Modersitzki, J., 2003, Numerical methods for image registration: Oxford University Press.

Nabighian, M. N., and J. C. Macnae, 1991, Time domain electromagnetic prospecting methods, *in* M. N. Nabighian, ed., Electromagnetic methods in applied geophysics: SEG, 427–520.

Oldenburg, D. W., E. Haber, and R. Shekhtman, 2013, Three dimensional inversion of multisource time domain electromagnetic data: Geophysics, **78**, no. 1, E47–E57, doi: 10.1190/geo2012-0131.1.

Osher, S., and R. P. Fedkiw, 2001, Level set methods: An overview and some recent results: Journal of Computational Physics, **169**, 463–502, doi: 10.1006/jcph.2000.6636.

Osher, S., and J. A. Sethian, 1988, Fronts propagating with curvature-dependent speed: Algorithms based on Hamilton-Jacobi formulations: Journal of Computational Physics, **79**, 12–49, doi: 10.1016/0021-9991(88)90002-2.

Palacky, G. J., 1988, Resistivity characteristics of geologic targets, *in* M. N. Nabighian, ed., Electromagnetic methods in applied geophysics: SEG, 53–129.

Pidlisecky, A., K. Singha, and F. D. Day-Lewis, 2011, A distribution-based parametrization for improved tomographic imaging of solute plumes: Geophysical Journal International, **187**, 214–224, doi: 10.1111/j.1365-246X.2011.05131.x.

Prikhodko, A., T. Eadie, N. Fiset, and L. Mathew, 2012, VTEM (35 m) test results over the Caber and Caber North deposits (October 2012): Technical report.

Prikhodko, A., E. Morrison, A. Bagrianski, P. Kuzmin, P. Tishin, and J. Legault, 2010, Evolution of VTEM — Technical solutions for effective exploration: Presented at ASEG 21st International Geophysical Conference and Exhibition.

Raiche, A. P., 1998, Modelling the time-domain response of AEM systems: Exploration Geophysics, **29**, 103–106, doi: 10.1071/EG998103.

Reynolds, J. M., 1998, An introduction to applied and environmental geophysics: John Wiley & Sons.

Tai, X.-c., and T. F. Chan, 2004, A survey on multiple level set methods with applications for identifying piecewise constant functions: International Journal of Numerical Analysis and Modeling, **1**, 25–47.

van den Doel, K., and U. Ascher, 2006, On level set regularization for highly ill-posed distributed parameter estimation problems: Journal of Computational Physics, **216**, 707–723, doi: 10.1016/j.jcp.2006.01.022.

Ward, S. H., and G. W. Hohmann, 1988, Electromagnetic theory for geophysical applications, *in* M. N. Nabighian, ed., Electromagnetic methods in applied geophysics: SEG, 131–311.

Xiong, Z., and A. C. Tripp, 1995, A block iterative algorithm for 3D electromagnetic modeling using integral equations with symmetrized substructures: Geophysics, **60**, 291–295, doi: 10.1190/1.1443757.